applied sciences

IMPACT FACTOR 2.7

CITESCORE 4.5

Article

Plasma Expansion Characterization of a Vacuum Arc Thruster with Stereo Imaging

Roman Forster, Carmen Kirner and Jochen Schein

Special Issue
Recent Advances in Space Propulsion Technology

Edited by
Prof. Dr. Jason Cassibry and Dr. Nathan Schilling

MDPI

https://doi.org/10.3390/app13052788

applied sciences

MDPI

Article

Plasma Expansion Characterization of a Vacuum Arc Thruster with Stereo Imaging

Roman Forster *, Carmen Kirner and Jochen Schein *

Institute for Plasma Technology and Basics of Electric Engineering, Bundeswehr University, 85579 Neubiberg, Germany

* Correspondence: roman.forster@unibw.de (R.F.); jochen.schein@unibw.de (J.S.)

Abstract: In order to support increasingly detailed simulation models in the field of plasma generation and expansion, more experimental data are needed to prove and verify these models. In addition to existing invasive probe methods and spectroscopy, optical diagnostics methods can be employed for this purpose. These can be used to obtain information about the transient behavior of the plasma plume itself. For this purpose, a pseudo stereo imaging system was assembled, which consisted of a biprism and one camera. The presented setup was used to observe the plasma plume expansion of a vacuum arc thruster and to detect how a magnetic nozzle changes the plume expansion behavior of the used thruster. For this, areas were calculated by means of contour detection from both view directions, and a 3D model was reconstructed by computing cross-sectional images. The results show that the magnetic nozzle provides a more uniform formation of the plasma plume, which can be seen by comparing the calculated areas from both directions of observation and is confirmed by the reconstructed 3D models. Thus, the used setup is suitable as an additional diagnostic tool in the future. Despite its simple design, it provides information about the spatial development of a plasma plume. It can serve as a fast and simple verification tool for simulation results, where otherwise complex tomographic setups and reconstructions would be necessary to obtain spatial information. Further measurements are recommended to improve and validate the recording and evaluation process.

Keywords: vacuum arc thruster; PJP; magnetic nozzle; stereo imaging; plasma

Citation: Forster, R.; Kirner, C.; Schein, J. Plasma Expansion Characterization of a Vacuum Arc Thruster with Stereo Imaging. *Appl. Sci.* **2023**, *13*, 2788. https://doi.org/10.3390/app13052788

Academic Editor: Emilio Martines

Received: 27 January 2023
Revised: 15 February 2023
Accepted: 17 February 2023
Published: 21 February 2023

1. Introduction

In many applications, a trend towards smaller and more flexible satellite systems can be observed. Mass and volume savings reduce launch and mission costs, making expeditions possible for smaller companies or research institutions. On the one hand, this miniaturization is possible due to innovatively developed electronics and, on the other hand, due to the use of smaller and lighter propulsion systems, which usually account for a considerable proportion of the satellite's total mass and are thus a major factor in high mission costs [1–3].

For microsatellites, the vacuum arc thruster (VAT) has established itself as a simple, low-mass and fairly robust propulsion system. The mode of operation is based on a pulsed vacuum arc discharge generated between two electrodes separated by an isolator. The VAT is a solid fuel thruster because it uses a solid cathode material (usually a metal) as a propellant. After ignition at so-called cathode spots, this material is vaporized and ionized, and the expansion of these spots creates a small impulse bit. This simplicity and the ability to easily scale the thrust up and down by simply changing the repetition rate make the VAT promising as an economically priced, compact propulsion system for microsatellites [4–7]. There are two ways to initiate a discharge. There is the so-called triggerless mode, in which a low-resistance conductive layer exists between the cathode and anode on the insulator;

alternatively, there is the trigger mode, which ensures a breakdown and thus a discharge by means of an applied high voltage between the two electrodes [8–10].

By applying an external magnetic field, which is operating as a magnetic nozzle, the thrust to power ratio of the thruster can be improved. The magnetic field interacts with the charged particles and accelerates them towards the nozzle exhaust. In previous studies, the influence of external magnetic fields on VAT performance has been demonstrated [5,6,11–13].

In order to gain a more detailed insight into the complex processes of a vacuum arc and to study its behavior, many simulations have already been carried out [14–16]. However, there are still analytic measurements necessary that have been used for the characterization of VATs in the past. Parameters such as plasma potential, ion currents and ion velocities are commonly measured via probes [9,17,18]. Ion or electron densities are determined by means of Faraday cups [19]. Moreover, there are optical diagnostics such as observing cathode spots or arc evolution [1,11,20].

The goal in the European Union's Horizon 2020 research and innovation program was the development of a commercially successful VAT integrated into the so-called plasma jet pack (PJP). For the development and improvement of this design, simulation as well as the acquisition of experimental data are necessary to obtain a better idea of the operating system and to locate improvement potential [17,21]. The experimental data are also the basis for an attempted simulation of the system in the project. Numerous plasma diagnostic measurements from other project participants were supplemented with the results of the optical diagnostic investigated in this work. The goal of this study was to observe the expansion of the plasma plume and whether and how the PJP discharge can be manipulated by means of a magnetic nozzle. To obtain three-dimensional information about the plasma plume's expansion, tomographic measurement techniques have been used in previous research. This has been achieved by elaborate measurement setups and reconstruction algorithms [22–25]. In addition, there have already been other approaches to observe the plume expansion [26,27].

The idea of the present work was to use a less costly measurement setup to generate a three-dimensional reconstruction of the plume propagation. For this purpose, a pseudo stereo imaging system consisting of one camera with a biprism was assembled, giving us a temporally synchronized view from two directions. These were orthogonal to each other and could be transferred into a 3D projection by using one single high-speed camera with sufficient spatial resolution of the plasma plume [28–30]. These measurements were performed for both cases, with and without a magnetic nozzle.

2. Materials and Methods

2.1. VAT-Comat

The VAT studied in this work is a prototype of the plasma jet pack (PJP) from the French company Comat [31]. It is essentially a 30 W VAT, which is electrically driven by means of a capacitor bank [32]. A high-voltage trigger system allows the PJP to operate in both trigger and triggerless mode. A voltage of 250 V is applied between the two electrodes. After successful ignition, a high current up to 4 kA discharge occurs with a discharge duration of around 25 µs [17].

Figure 1 shows the PJP used in our experiments. From above, the anode can be seen as a cross. Copper was used as the anode material. The cathode and insulator were fixed concentrically to the anode exhaust. Copper was also used as a cathode material. The high-voltage trigger is separated from the cathode by an insulator and is in the center of the insulator in the form of a metal tip. On the back of the enclosure, the PJP is supplied with power and triggers signals via a Sub-D9 connector. The cable is connected to a lab power supply and frequency generator via a vacuum feedthrough. The VAT was supplied with a supply voltage of 14 V and triggered with a frequency of 1 Hz according to the manufacturer's instructions.

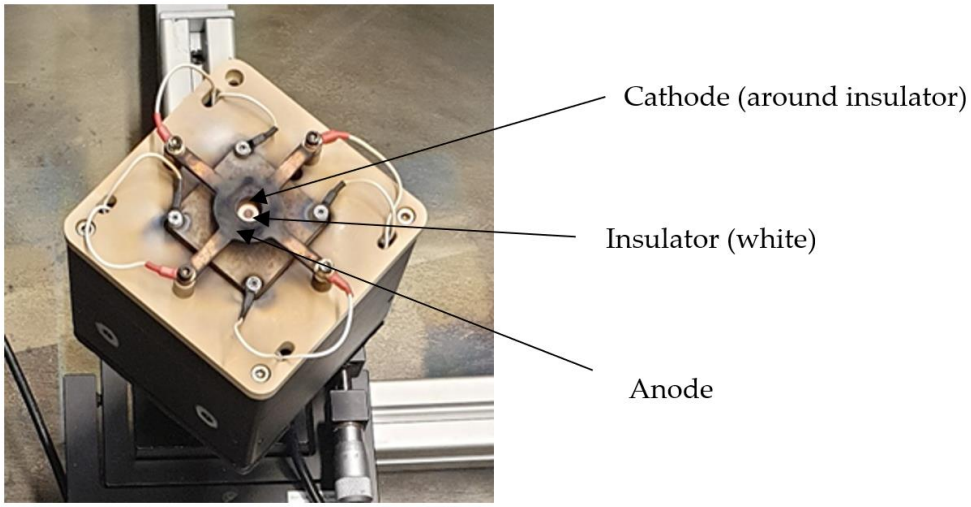

Figure 1. The used PJP model mounted centrally in the vacuum chamber.

For the measurements with a magnetic nozzle, an assembly based on a permanent magnet was used.

The body of the magnetic nozzle is made of peek. This material is suitable for containing the N45-neodymium permanent magnet due to its heat resistance and non-conductivity. The magnet had a remanence of 1.33–1.36 T axial magnetization direction and was formed as a ring with an inner diameter of 15 mm, an outer diameter of 25 mm and a height of 6 mm, as can be seen in Figure 2a. The nozzle system was clamped to the anode by means of nylon screws connecting a small peek plate and the peek body of the magnet. The circular opening of the nozzle was adapted concentrically to the anode according to Figure 2b.

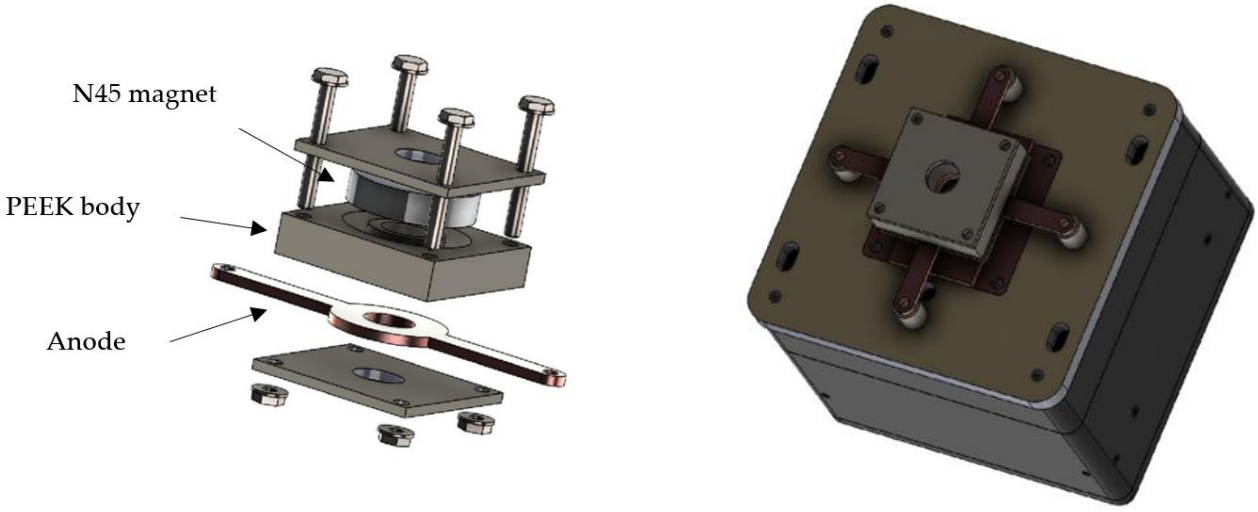

Figure 2. Magnetic nozzle used: (**a**) exposure view of the nozzle system; (**b**) CAD model of PJP with mounted magnetic nozzle.

2.2. Periphery

The periphery of the entire measurement setup consists of a vacuum chamber with suitable vacuum pumps, a high-speed camera for image recording, the PJP including a power supply and a control unit for triggering.

A vacuum chamber with a diameter of 80 cm and a height of 70 cm, equipped with four optical inlets with a diameter of 21 cm on each side, was used. Furthermore, there

are several electrical feedthroughs, to connect the VAT to the power supply and trigger system. A rotary valve pump and a turbomolecular pump were used, providing constant vacuum levels of approximately 10^{-6} mbar. The required power of 30 W for the PJP was supplied by a Voltcraft vlp-1302a power supply, while the waveform generator LXI G5100A, manufactured by Picotest, Phoenix, AZ, USA, ensured the triggering of the ignition. For recording, a Dimax HS4 high-speed camera was used. Excelitas PCO GmbH, Kehlheim, Germany, manufactured the mentioned camera. Additionally, a pulse delay generator DG645 was integrated into the triggering system, manufactured by Scientific Instruments GmbH, Gilching, Germany.

In Figure 3, the schematic drawings of the devices used and their connections are shown. The waveform generator triggers the PJP directly and the high-speed camera via the pulse delay generator. By means of the pulse delay generator, it is possible to set a desired value between the ignition of the thruster and the start of the recording of the camera. Thus, it is possible to take images at specific points in time of the discharge. This means that, additionally, the time course of the spatial evolution of the plasma plume can be observed. From this, the spatial expansion of the plasma can be obtained at desired points in time.

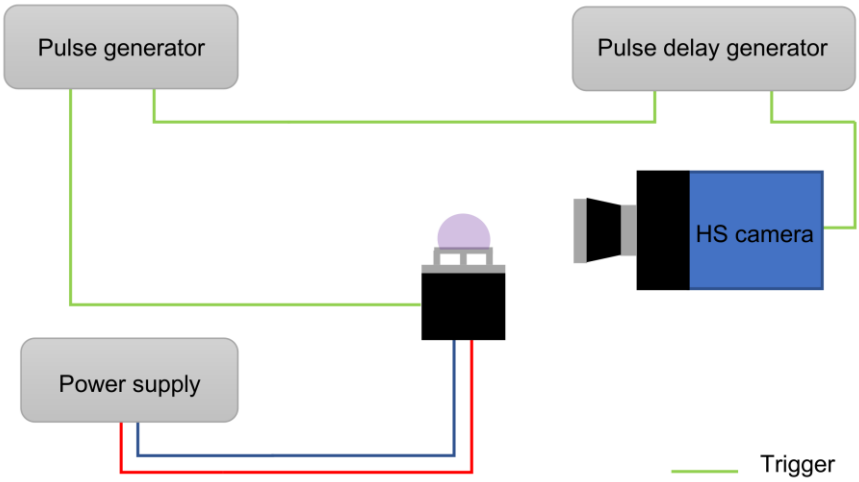

Figure 3. Schematic of the controlling and triggering system. The red and blue lines are the power supply and the green line is the trigger.

As can be seen in Figure 4, the VAT was placed in the center of the chamber. To ensure recordings from two directions of observation, orthogonally from each other, the thruster was mounted with the electrodes facing upwards. Via two deflection mirrors and a biprism mounted immediately in front of the high-speed camera, synchronized imaging from two observation planes is possible. The used biprism was a 90° specialty mirror with 50 mm legs and a 70.7 mm hypotenuse. It was enhanced by an aluminum coating with an average reflectance of >95% at 450–650 nm and an angle tolerance of ±2°. The surface flatness amounted to λ/4 and the surface quality to 40–20. Both deflection mirrors were also enhanced with aluminum coating with an average reflectance of >95% at 450–650 nm at an angle of 45°. The surface flatness amounted to 4–6 λ and the surface quality to 60–40. Both deflection mirrors had a size of 50 mm × 75 mm. All mirrors were manufactured by Edmund Optics Inc., Barrington, NJ, USA. The CMOS image sensor of the used high-speed camera with a resolution of 2000 × 2000 pixel had a maximum frame rate of 2277 fps at full resolution. The dynamic range of the camera amounted to 12 bits.

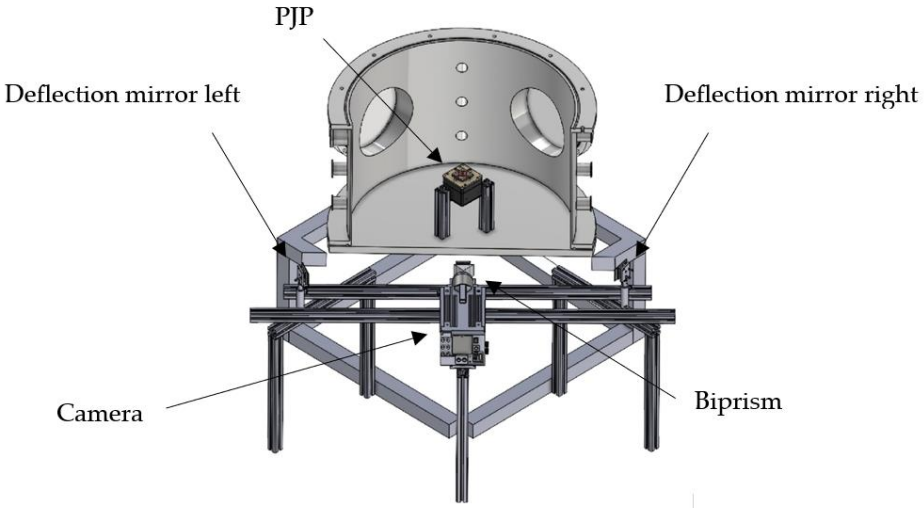

Figure 4. Vacuum chamber with PJP and arrangement of the used optical measurement system.

The entire optical setup, including all mirrors and the camera, was mounted on aluminum structural profiles and an optical rail system and was attached to the base of the vacuum chamber. To ensure a proper line for recording, all components were aligned in the center of the two windows. Care was also taken to ensure that the optical path was the same length in both directions of observation. The deflection mirrors and the biprism were mounted on specific holders so that fine adjustment could be made both vertically and horizontally. These kinematic mirror mounts were produced by OWIS GmbH, Staufen, Germany.

2.3. Stereo Imaging System

A modified stereo imaging system was used in this work. Instead of the more common setup with two cameras, one camera observed the thruster from two perspectives via a biprism and two deflection mirrors.

Figure 5 illustrates the modified stereo-optical measurement setup. By means of this setup, it is possible to detect the measurement object in two planes at the same time, so that a temporally synchronized spatial detection is realized. Thus, a simplified three-dimensional reconstruction of the measurement object can be made. Precise alignment and adjustment of the optical setup is required. For this purpose, the whole setup was aligned to the position of the thruster, which was mounted centrally in the vacuum chamber and at half the height of the chamber windows. The thruster was arranged with a rotation by 45° to prevent the anode mounting spacers and screws from entering the optical path between the PJP exit and the camera. Both deflection mirrors were placed at the same distance from the optical path, which had a length of approximately 1400 mm. Finally, the biprism and camera were positioned centrally between both deflection mirrors. Due to the small size of the measuring object compared to the recording distance and the resulting small solid angle, the possible distortion of the recorded images can be considered negligible. However, a quantitative statement cannot be made for this. In summary, it can be said that this setup impresses with its simplicity. Only a few mirrors and a triggerable camera are needed. Thus, a time-synchronized measurement is possible. In addition, this system can be combined with other diagnostic techniques easily due to its trigger ability. The simple scalability of the system is also advantageous. In contrast, only the complex and precise positioning and alignment of the optical components is required, which is more demanding for larger measuring distances, as in this case, than for smaller measuring distances.

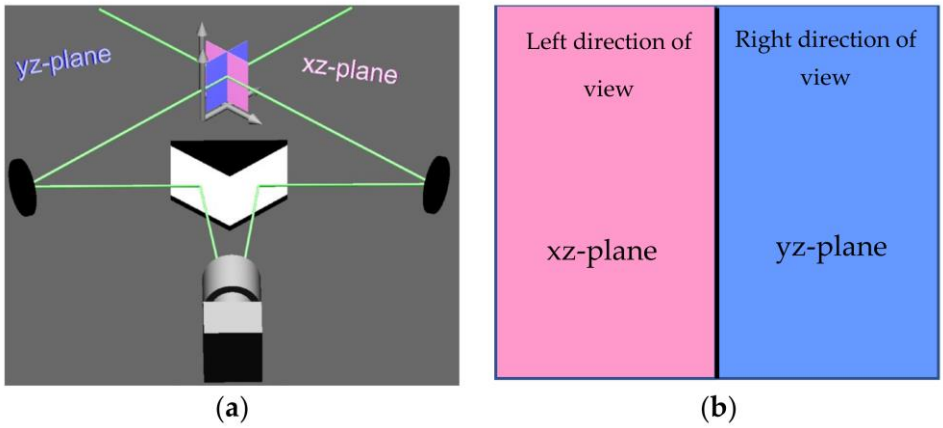

Figure 5. Schematic principle of the used stereo-optical measurement system: (**a**) schematic layout of camera and mirrors; (**b**) scheme of the divided CMOS camera chip.

2.4. Adjustment of the Stereo Imaging System

Before data acquisition could start, the optical components had to be precisely adjusted. The rough positioning is described in the previous section. For exact alignment of the optical elements, the thruster was observed using backlight illumination. By means of the fine adjustment option of the kinematic mirror mounts, the images of the thruster could be aligned very precisely, so that there was no misalignment between the two views of observation.

In Figure 6, the result of the fine adjustment can be seen. It can be recognized that there is no vertical offset between the left and right directions of view, because the upper boarder of the PJP chassis is located at the same height.

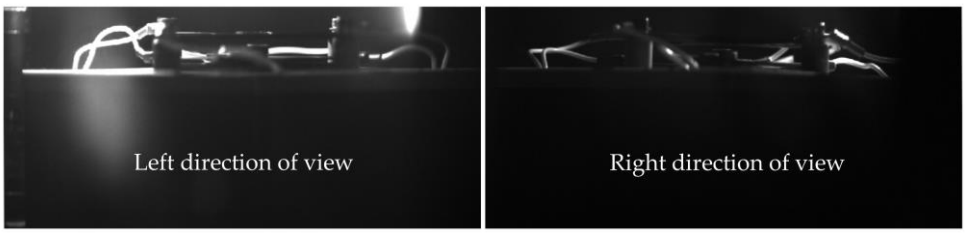

Figure 6. Recorded image after adjustment of the system. The white line in the middle of the image symbolizes the separation of the camera chip according to Figure 5b.

2.5. Data Acquisition and Processing

The following describes the process of the acquisition and processing of the images and data.

The operating frequency of the PJP was set to 1 Hz. The maximum resolution of the camera, 2000 × 2000 pixel, was used for all recordings. An exposure time of 1.5 µs was set for all measurements. The recording of the ignition was time-synchronized with a variable time delay, which considered the temporal offset between the ignition of the thruster and the start of the camera recording. The measurements were done with and without a magnetic nozzle.

The delay values listed in Table 1 were used. Since the maximum discharge current was measured after 10 µs in the studies of other project participants, the plume expansion was sampled up to this point. One hundred images were recorded for all set values. In the following, the acquisition and evaluation process is described using the example of acquisition and recording from the setup without a magnetic nozzle. The procedure for measurements with a magnetic nozzle was identical.

Table 1. Used time delay values for the measurements.

Value	Unit
10	ns
500	ns
750	ns
1	µs
10	µs

The recording in Figure 7 displays the illustration of the discharge from two directions of view on the divided camera chip. The left one corresponds to the left direction of view in Figure 5 and the right one to the right direction of view. From this recording, the scale factor for the later calculation can be determined by using the observed size of the anode, too. For this purpose, the dynamic range of the recorded image was adjusted in such a way that the thickness of the anode could be determined in pixels. With the known dimensions of the anode, a scaling factor in $\frac{mm}{Px}$ could be calculated.

Figure 7. Recorded image of the ignition from the PJP without magnetic nozzle with 1 µs time delay. On the left side of the camera chip, the left direction of view is mapped, and on the right side, the corresponding right direction of view.

For further processing, a region of interest (ROI) from both observations was cropped from the camera image to reduce the calculation effort. Both sections had an identical size. The snippets were positioned manually, so that the lower border of the ROIs overlaid with the upper border of the cathode. The ROIs were placed horizontally, so that the cathode was centered. To be able to calculate the area of the plasma, the shape and expansion of the plume must be determined.

The expansion of the plasma plume was calculated by extracting the contours from both extracted ROIs. In Figure 8, two contours are displayed. On the left side, the sector from the left direction of observation is shown, and on the right side, correspondingly from the right direction of observation. The contours of the plasma plume were sliced using a well-known algorithm called "marching cubes". The areas of the sectors using the previously determined scale factor could be calculated.

(**a**) (**b**)

Figure 8. Assigned contours of the cropped ROIs from Figure 7 for calculating the plume area: (**a**) left direction of view; (**b**) right direction of view.

To calculate a 3D model, both sectors were used to calculate a cross-sectional image from both perspectives.

$$\begin{pmatrix} x_1 \\ \vdots \\ x_m \end{pmatrix} * \begin{pmatrix} y_1 & \cdots & y_n \end{pmatrix} = \begin{pmatrix} x_1 * y_1 & \cdots & x_1 * y_n \\ \vdots & \ddots & \vdots \\ x_m * y_1 & \cdots & x_m * y_n \end{pmatrix} \quad (1)$$

The cross-sectional image is a dyadic matrix product of both vectors, representing one line in the left and right observation, respectively. Due to the orthogonality of the two directions of observation, one vector can be considered as a single column matrix ($\underset{x}{\rightarrow}$ in Figure 9a and the other as a single row matrix ($\underset{y}{\rightarrow}$ in Figure 9c). The resulted matrix product from Equation (1) describes the two-dimensional cross-sectional image, which can be seen in Figure 9b.

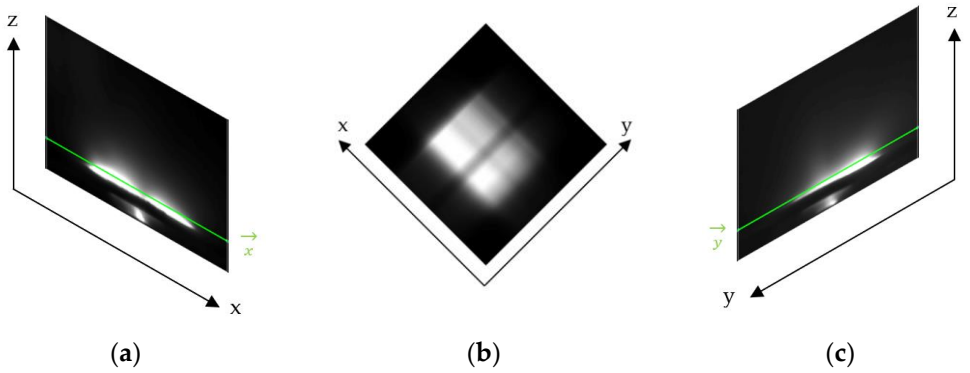

Figure 9. Graphical principle of cross-sectional image calculation from the two viewing directions: (**a**) left observation; (**b**) calculated cross-sectional image; (**c**) right observation.

Figure 9 is a graphical representation of the procedure for calculating an exemplary cross-sectional image. For every line in both sectors, a cross-sectional image is calculated. In Figure 9b, the cross-sectional image from the green lines in (a) and (c) is shown. The line number in the left and right image is always identical.

To obtain a three-dimensional structure, both sectors were scanned simultaneously line by line. For every line, the corresponding cross-sectional image was calculated. These images were then stacked on each other, which leads to a three-dimensional matrix. The following figure explains this procedure graphically.

In Figure 10, the calculation of the 3D model is graphically presented. Both sectors were scanned line by line starting at z = 0. Two lines are shown in (a) and (c) as an example. Both green lines correspond to the same line number and both red lines accordingly. For each vector pair, x and y, a cross-sectional image is computed. The green-bordered cross-sectional image in (b) is the dyadic matrix product of x_1 and y_1 and the red one of x_2 and y_2. To visualize the reconstruction more clearly, cross-sectional images of two non-neighboring lines are shown. Thus, the layer by layer formation of the 3D structure is easier to understand. All cross-sectional images have to stack on top of each other starting from z = 0 to the height of the sections, to calculate the complete 3D model. The computed 3D models were normalized to 8 bits.

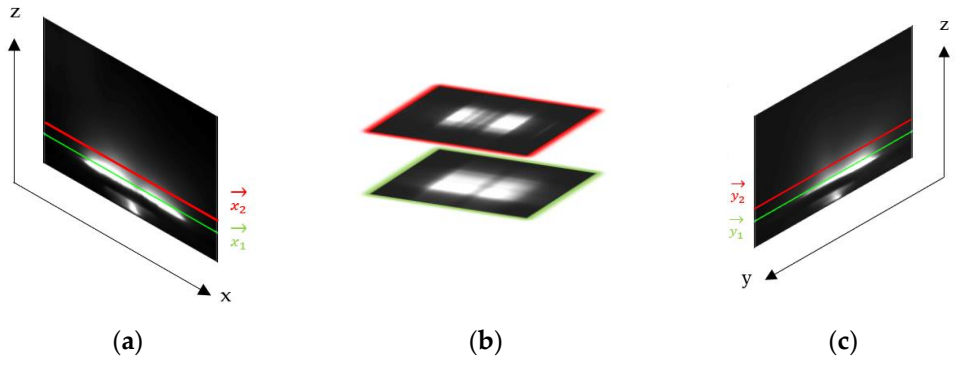

Figure 10. Schematic of the reconstruction of the 3D model: (**a**) left observation with two lines; (**b**) the two calculated cross-sectional images from the lines in (**a**,**c**); (**c**) right observation with two lines.

3. Results

First, the results of the calculation of the are shown, followed by the reconstructed 3D models.

Figure 11 shows two diagrams with the results from the calculation of the area of the plume expansion. For all points in time, the mean value of the recordings was calculated and is displayed with the standard deviation as an error bar. The partly large deviations and discrepancies originate from the highly non-uniform discharge of the thruster. This fluctuation in the formation of the plasma jet was also found in studies by project participants [17]. Graph (a) shows the calculated values at the mentioned points in time from Table 1 without a nozzle, and (b) shows the values when using a magnetic nozzle. It can be seen that when increasing the time distance between the ignition of the thruster and recording of the images, the calculated areas increase in both cases as well. This seems plausible based on the PJP discharge duration of 25 µs. The calculated areas for the setup without a magnetic nozzle show higher values within a delay of 750 ns between ignition and image acquisition. For a delay higher than 750 ns, the setup with a magnetic nozzle shows higher values.

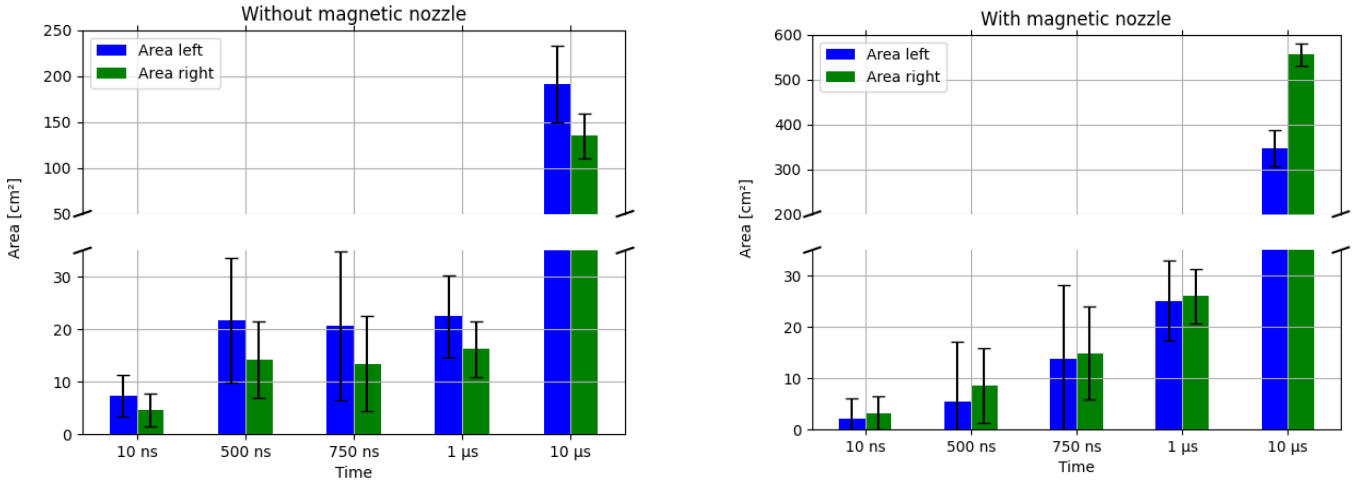

(**a**) (**b**)

Figure 11. Calculated areas (blue: left direction of observation; green: right direction of observation) from the sliced contours of both perspectives: (**a**) thruster without magnetic nozzle; (**b**) thruster with magnetic nozzle.

Essentially, the values indicate a more uniform shape formation when using a magnetic nozzle, because of the lower percentage deviation between both directions of observation. Only for the 10 µs point in time, a higher deviation between the calculated areas of both directions of observation can be recognized. The reason for this is physical-based, because a qualitative difference in the plume expansion is already recognizable in the recordings of Figure 12b for instance, which is confirmed by the different area values for the setup without a magnetic nozzle. Furthermore, a more homogenous qualitative expansion of the plume as in Figure 13b demonstrates a small deviation in the area values of both directions of view for the setup with a magnetic nozzle. These observations are confirmed by the other recordings in Figures 14 and 15b,e,h.

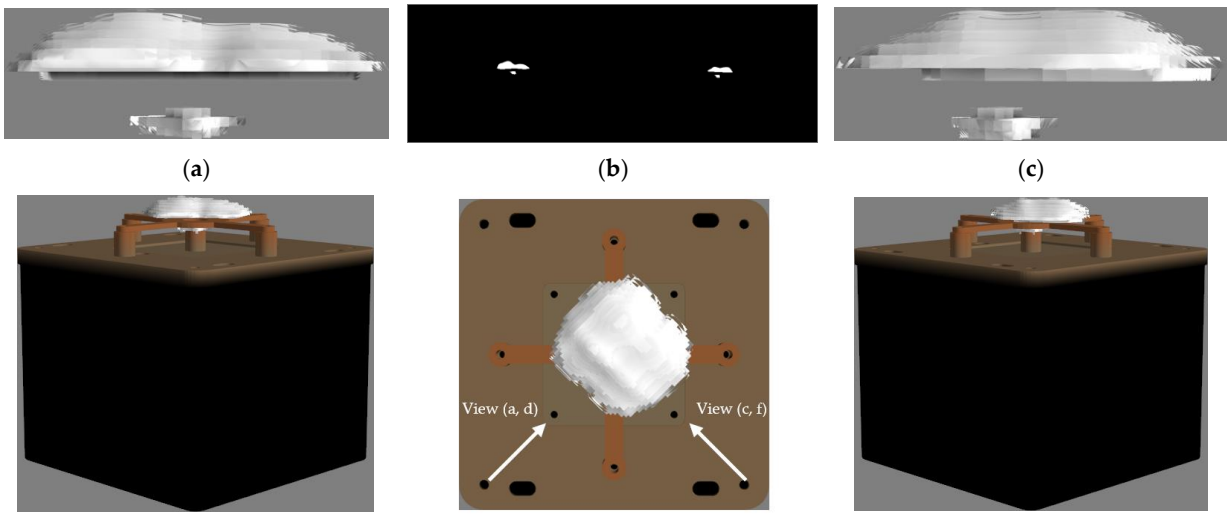

(**a**) (**b**) (**c**)

(**d**) (**e**) (**f**)

Figure 12. Calculated 3D models of the plasma plume at 1 µs without magnetic nozzle and with the PJP model: (**a**) reconstructed plume left direction of observation; (**b**) recorded image with both directions of observation; (**c**) reconstructed plume right direction of observation; (**d**) isometric view of left direction of observation with PJP; (**e**) front view with PJP; (**f**) isometric view of right direction of observation with PJP.

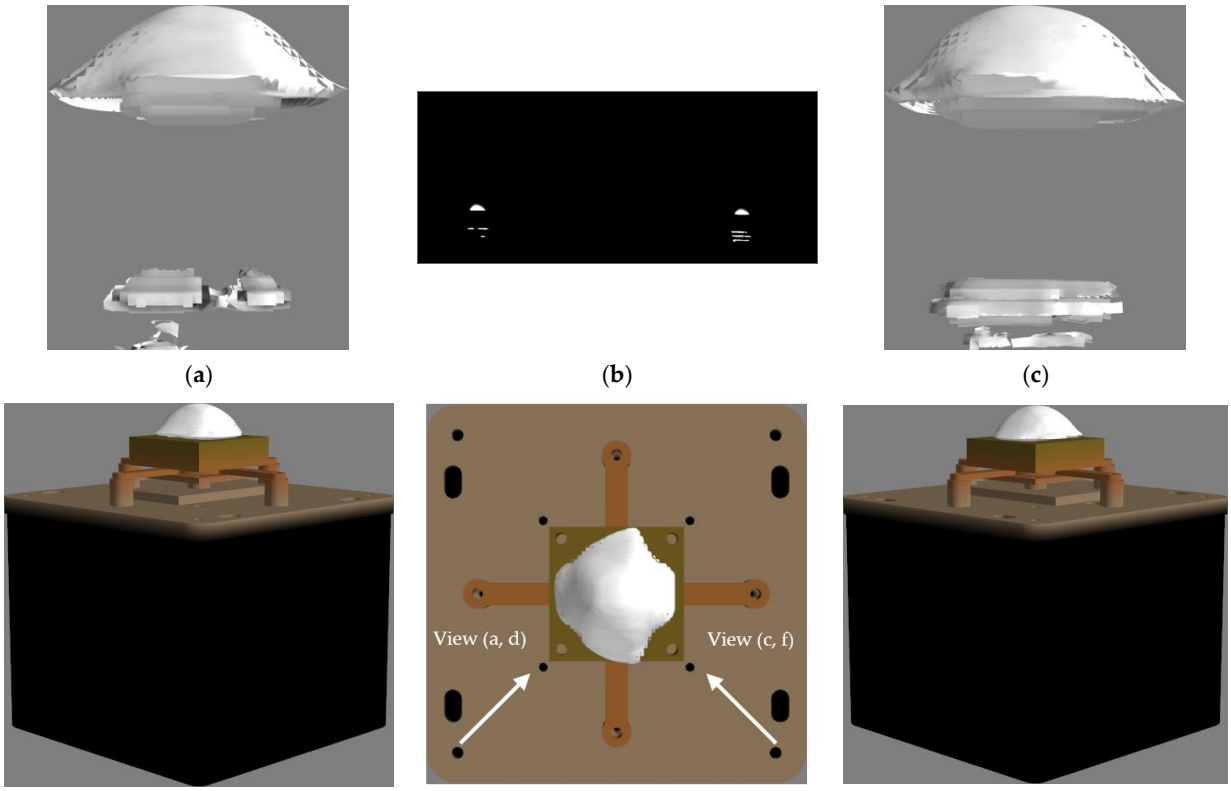

(**a**) (**b**) (**c**)

(**d**) (**e**) (**f**)

Figure 13. Calculated 3D models of the plasma plume at 1 µs with magnetic nozzle and with the PJP model: (**a**) reconstructed plume left direction of observation; (**b**) recorded image with both directions of observation; (**c**) reconstructed plume right direction of observation; (**d**) isometric view of left direction of observation with PJP; (**e**) front view with PJP; (**f**) isometric view of right direction of observation with PJP.

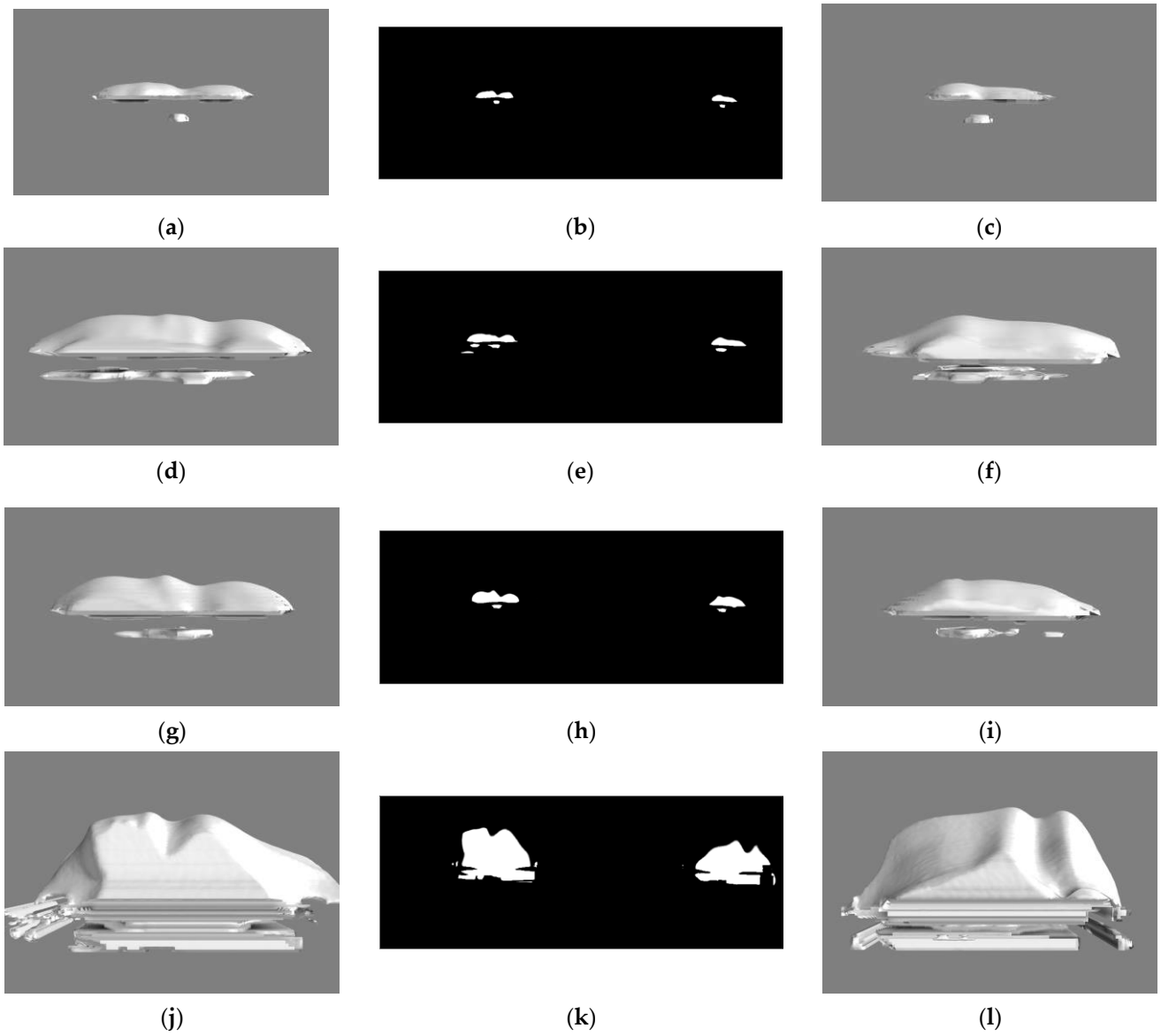

Figure 14. Results for all measurements without magnetic nozzle: (**a**) left direction of observation 10 ns; (**b**) recording 10 ns; (**c**) right direction of observation 10 ns; (**d**) left direction of observation 500 ns; (**e**) recording 500 ns; (**f**) right direction of observation 500 ns; (**g**) left direction of observation 750 ns; (**h**) recording 750 ns; (**i**) right direction of observation 750 ns; (**j**) left direction of observation 10 µs; (**k**) recording 10 µs; (**l**) right direction of observation 10 µs.

By comparison to the discharge current, a correlation between the discharge current and the plume area can be recognized [17]. The correlation is valid tendentially for both cases, with and without a magnetic nozzle, whereas the use of the magnetic nozzle shows a stronger increase in area.

These conclusions from the above figures were investigated additionally by computing a 3D model from both perspectives.

Figure 12 shows the calculated 3D model of the plasma plume for the setup of ignition without a magnetic nozzle. This model was computed from recording 1 µs after ignition, seen in (b). While (a) represents the left perspective, (c) shows the right direction of view. To obtain a better spatial idea of the reconstructed model, the 3D model of the PJP was included and an isometric view of the reconstruction is shown. The front view of the plume together with the PJP is shown in (e), while (d) represents the isometric view of the left direction of observation and (f) shows the corresponding right view with the 3D

PJP model, respectively. Considering the recording of the two perspectives, the shape can be recognized in the corresponding reconstructed 3D model. As the recordings and the models show, the shape of the plasma plume is not uniform, because of the clearly different expansion shape observed from the two perspectives.

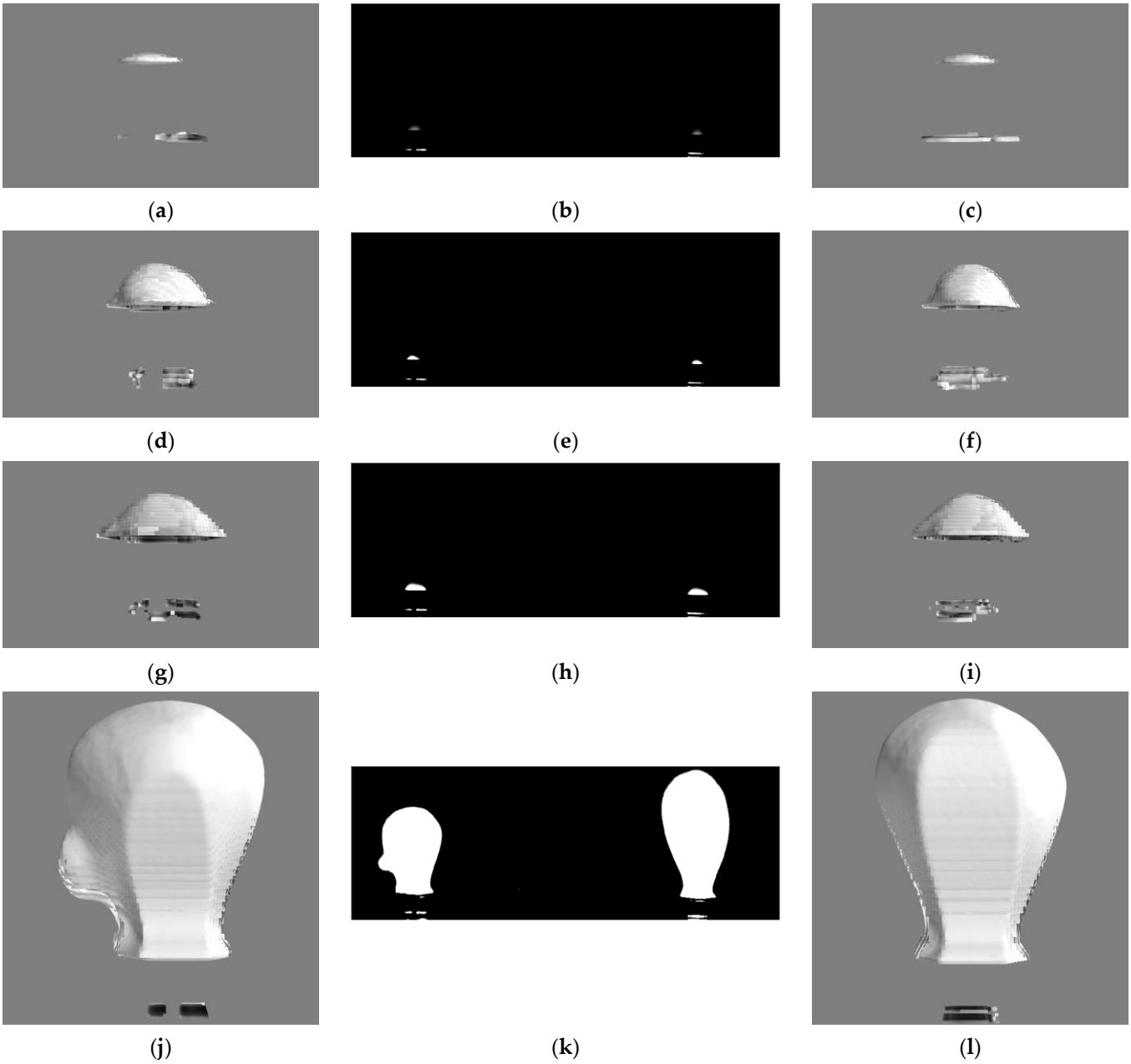

Figure 15. Results for all measurements with magnetic nozzle: (**a**) left direction of observation 10 ns; (**b**) recording 10 ns; (**c**) right direction of observation 10 ns; (**d**) left direction of observation 500 ns; (**e**) recording 500 ns; (**f**) right direction of observation 500 ns; (**g**) left direction of observation 750 ns; (**h**) recording 750 ns; (**i**) right direction of observation 750 ns; (**j**) left direction of observation 10 µs; (**k**) recording 10 µs; (**l**) right direction of observation 10 µs.

In Figure 13, the corresponding results of the evaluation from measurements 1 µs after ignition with a magnetic nozzle are illustrated. The arrangement of the images is identical to that in Figure 12. Here, the model of the thruster with the magnetic nozzle is also displayed. An isometric view of the reconstructed model is also shown in (d) and (f) to offer a spatial impression of the result. Here, the more uniform shape of the plasma plume

can be detected. By comparing the results from Figures 12 and 13, it can also be seen that the plasma shows greater expansion along the nozzle exit when using the magnetic nozzle.

To detect the plume expansion at several points in time, the camera recorded images with a set delay according to Table 1. For all recordings, a 3D model was computed.

Figure 14 shows the recorded images and the corresponding reconstructed 3D models for the other measurements—10 ns, 500 ns, 750 ns and 10 µs after iginition—and without a magnetic nozzle. In this figure, the 3D model of the PJP is omitted for clarity. The formation of the plasma plume is very irregular. This can be seen from the recordings (b), (e), (h) and (k). They do not show the homogeneous and uniform formation of the plasma plume. Rather, clear irregularities and incisions are visible on the contour of the plume. The calculated three-dimensional models reproduce these obvious features well. It can be seen that the discharge spreads preferably horizontally at the beginning. Only after a longer time interval from ignition does the plume expand increasingly vertically.

The corresponding 3D models using the magnetic nozzle for the different points in time were also calculated.

In Figure 15, the results for the measurements with a magnetic nozzle are listed. The arrangement is identical to that in Figure 14. The gap in the images and the 3D models presents the magnetic nozzle, as can be seen in Figure 13. The recordings (b), (e) and (h) and the reconstructed models show that the formation of the plume is more homogeneous than for the measurements without a magnetic nozzle. It can also be recognized that the plume expands preferentially vertically and spreads further with an increasing time interval to the ignition in comparison to the case using no magnetic nozzle.

Looking at all calculated 3D models, it can be said that the shape and features of the plasma plume can be reconstructed from both directions of observation. It should be noted that the reconstruction does not offer a detailed and accurate model. This would require significantly more directions of observation. Therefore, it is called a simplified 3D model. This would lead to a more complex measurement setup and data processing, which is one advantage of the used setup. The models also confirm the conclusion that the plume shape is more uniform when using the magnetic nozzle. It is also obvious that the plasma expansion along the PJP outlet is larger, when the magnetic nozzle is mounted.

4. Discussion

The plasma plume expansion of a 30-W class vacuum arc thruster was investigated by means of high-speed 3D imaging. The VAT was operated with and without a magnetic nozzle (~1.3 T). The recordings were done by a pseudo stereo imaging system with a biprism, to reduce the system to one single camera, which simplifies the handling of the recording. By means of this imaging system, the VAT was observed from two observation directions, which were oriented orthogonally to each other. The areas of the expanded plasma plume were calculated and a simplified 3D model was computed to obtain information about the shape of the plasma plume.

The results from calculating the areas of the plume expansion show that the PJP discharge is significantly influenced by the application of an external magnetic field. When the magnetic nozzle was mounted, the calculated plume area became significantly larger with time compared to the unmagnetized operation, as the results of recording 1 µs and 10 µs after thruster ignition show. For the points in time that are closer than 1 µs to the ignition, the results for the setup with the magnetic nozzle indicate a smaller area than for the setup without the magnetic nozzle. This seems consistent with the results of previous works, where, with an increasing magnetic field, the axial plume expansion decreases. However, in these investigations, lower magnetic fields in the range <0.3 T and arc currents lower than 1 kA were used [5,6]. The PJP operates in the same current regime only during the first µs after ignition; an arc current of less than 1 kA is also detected within 1 µs after ignition, while it increases exponentially in 10 µs to approximately 4 kA [17]. Thus, in the time range <1 µs, the PJP could be comparable to the thruster operated in previous works and the applied magnetic field is able to suppress the expansion of the plume. However,

with increasing temporal distance, the plume expansion magnifies due to the abruptly increased discharge current, when the plasma follows the expanding field lines at larger distances from the PJP surface.

The magnetic nozzle seems to support the more uniform formation of the plume, which can be seen by the calculated areas, which show lower deviations between the two perspectives, and furthermore by the reconstructed 3D models. The plume spreads further in the direction of the nozzle outlet in the case of the magnetic nozzle, while, without a magnetic nozzle, the expansion is lower and more horizontal regarding the nozzle outlet. The magnetic field is responsible for the consistent expansion, which was investigated in previous research [5,12].

The more uniform expansion of the plasma plume when using the magnetic nozzle is advantageous, as it reduces the fluctuations of the plasma jet formation. Thus, the pulse-by-pulse varying discharge can be cushioned.

For further research, it is recommended to investigate the influence of external magnetic fields on the PJP in more detail. The strength of the magnetic field as well as the position should be varied; hence, an electromagnet would be a good choice. Thrust measurements combined with ion current measurements should be used to validate the 3D investigations as this optical method is easy to apply and non-invasive.

5. Conclusions

In this work, the discharge of a VAT was investigated stereo-optically. For this purpose, the measured object was recorded simultaneously from two different viewing directions. The 3D models calculated from the recordings show the structure of the discharge. The optical setup presented here is characterized by its flexible, simple and cost-effective design, since only a few optical components are required. The non-invasive measurement methodology is also advantageous. Furthermore, the setup can be used in combination with other diagnostics at the same time. By selectively triggering the recording, the discharge can also be recorded at different points in time. For this reason, this diagnostic is suitable for checking and supplementing simulations, since the spatial expansion of the plasma and the temporal development of the discharge can be observed and compared with possible simulation data. Thus, the measurement methodology presented here can be considered as a complement to established plasma diagnostics, which are necessary to verify and check plasma simulations. For this, however, further investigations are necessary, comparing a created plasma model with the empirically determined results of this measurement technique.

Author Contributions: Conceptualization, R.F. and C.K.; methodology, R.F.; software, R.F.; validation, R.F., C.K. and J.S.; formal analysis, R.F. and J.S.; investigation, R.F.; resources, J.S.; data curation, R.F.; writing—original draft preparation, R.F. and C.K.; writing—review and editing, R.F., C.K. and J.S.; visualization, R.F. and C.K.; supervision, R.F. and J.S.; project administration, R.F. and J.S.; funding acquisition, J.S. All authors have read and agreed to the published version of the manuscript.

Funding: This research was funded by the European Union's Horizon 2020 research and innovation program under grant agreement No. 870444, Plasma Jet Pack project.

Institutional Review Board Statement: Not applicable.

Informed Consent Statement: Not applicable.

Data Availability Statement: Not applicable.

Conflicts of Interest: The authors declare no conflict of interest.

References

1. Pietzka, M.; Kirner, S.; Kauffeldt, M.; Arens, C.; Marques-Lopez, J.-L.; Forster, G.; Schein, J. Development of Vacuum Arc Thrusters and Diagnostic Tools. In Proceedings of the 32nd International Electric Propulsion Conference, Wiesbaden, Germany, 11–15 September 2011.
2. Pascoa, J.C.; Teixeira, O.; Filipe, G. A Review of Propulsion Systems for CubeSats. In Proceedings of the International Mechanical Engineering Congress and Exposition, Pittsburgh, PA, USA, 9–15 November 2018.
3. Schein, J.; Krishnan, M.; Shotwell, R.; Ziemer, J. Vacuum Arc Thruster for Optical Communications Mission. In Proceedings of the 39th AIAA/ASME/SAE/ASEE Joint Propulsion Conference and Exhibit, Huntsville, Alabama, 20–23 July 2003.
4. Kronhaus, I.; Laterza, M.; Maor, Y. Inline Screw Feeding Vacuum Arc Thruster. *Rev. Sci. Instrum.* **2017**, *88*, 43505. [CrossRef] [PubMed]
5. Chowdhury, S.; Kronhaus, I. Characterization of Vacuum Arc Thruster Performance in Weak Magnetic Nozzle. *MDPI Aerosp.* **2020**, *7*, 82. [CrossRef]
6. Keidar, M.; Schein, J.; Wilson, K.; Gerhan, A.; Au, M.; Tang, B.; Idzkowski, L.; Krishnan, M.; Beilis, I.I. Magnetically Enhanced Vacuum Arc Thruster. *Plasma Sources Sci. Technol.* **2005**, *14*, 661–669. [CrossRef]
7. Polk, J.E.; Sekerak, M.J.; Ziemer, J.K.; Schein, J.; Qi, N.; Anders, A. A Theoretical Analysis of Vacuum Arc Thruster and Vacuum Arc Ion Thruster Performance. *IEEE Trans. Plasma Sci.* **2008**, *36*, 2167–2179. [CrossRef]
8. Anders, A.; Brown, I.G.; MacGill, R.A.; Dickinson, M.R. 'Triggerless' Triggering of Vacuum Arcs. *J. Phys. D Appl. Phys.* **1998**, *31*, 584–587. [CrossRef]
9. Lun, J.; Dobson, R.T.; Steyn, W.H. Performance Measurements of a Medium-Current Short-Pulsed Vacuum Arc Thruster. *Exp. Technol.* **2014**, *38*, 6–16. [CrossRef]
10. Beilis, I. Vacuum Arc Ignition. Electrical Breakdown. In *Plasma and Spot Phenomena in Electrical Arcs*; Springer: Cham, Switzerland, 2020; pp. 143–164.
11. Keidar, M.; Zhuang, T.; Shashurin, A.; Teel, G.; Chiu, D.; Lukas, J.; Haque, S.; Brieda, L. Electric propulsion for small satellites. *Plasma Phys. Control. Fusion* **2015**, *57*, 14005. [CrossRef]
12. Xia, Q.; Wang, N.; Wu, X.; Xie, K.; Bai, S.; Zhang, Z.; Ren, L. The Influence of External Magnetic Field on the Plume of Vacuum Arc Thruster. *Acta Astronaut.* **2019**, *164*, 69–76. [CrossRef]
13. Zolotukhin, D.; Daniels, K.; Keidar, M. Discharge Characteristics of Two-Stage Micro-Cathode Arc MPD Thrusters with a Permanent Magnet and a Pulsed Magnetic Field. *J. Phys. D Appl. Phys.* **2021**, *54*, 15201. [CrossRef]
14. Shmelev, D.L.; Litvinov, E.A. The computer simulation of the vacuum arc emission center. *IEEE Trans. Plasma Sci.* **1997**, *25*, 533–537. [CrossRef]
15. Shmelev, D.L.; Barengolts, S.A.; Tsventoukh, M.M. Numerical Simulation of Plasma Near the Cathode Spot of Vacuum Arc. *IEEE Trans. Plasma Sci.* **2017**, *45*, 3046–3053. [CrossRef]
16. Delachaux, T.; Fritz, O.; Gentsch, D.; Schade, E.; Shmelev, D.L. Simulation of a High Current Vacuum Arc in a Transverse Magnetic Field. *IEEE Trans. Plasma Sci.* **2009**, *37*, 1386–1392. [CrossRef]
17. Michaux, E.; Mazouffre, S.; Blanchet, A. Time Evolution of Plasma Parameters in the Jet of a Low-Power Vacuum Arc Thruster. *J. Electr. Propuls.* **2022**, *1*, 7. [CrossRef]
18. Anders, A.; Yushkov, G.Y. Ion Flux from Vacuum Arc Cathode Spots in the Absence and Presence of a Magnetic Field. *J. Appl. Phys.* **2002**, *91*, 4824–4832. [CrossRef]
19. Lun, J.; Law, C. Influence of Cathode Shape on Vacuum Arc Thruster Performance and Operation. *IEEE Trans. Plasma Sci.* **2015**, *43*, 198–208. [CrossRef]
20. Zhou, Z.; Kyritsakis, A.; Wang, Z.; Li, Y.; Geng, Y.; Djurabekova, F. Direct Observation of Vacuum Arc Evolution with Nanosecond Resolution. *Sci. Rep.* **2019**, *9*, 7814. [CrossRef] [PubMed]
21. Garrigues, L.; Sarrailh, P. Generation of Multiply Charged Ions in the Context of a Vacuum Arc Thruster. In Proceedings of the 37th International Electric Propulsion Conference, Boston, MA, USA, 19–23 June 2022.
22. Wang, Z.; Pan, Y.; Zhang, W.; Li, H.; Geng, Y.; Wang, J.; Sun, L. An improved deep learning-based algorithm for 3D reconstruction of vacuum arcs. *Rev. Sci. Instrum.* **2021**, *92*, 123509. [CrossRef]
23. Wang, Z.; Pan, Y.; Gong, Y.; Cao, B.; Zhou, Z.; Sun, L.; Geng, Y.; Wang, J. 3D reconstruction of dynamic behaviors of vacuum arcs under transverse magnetic fields via computer tomography. *Rev. Sci. Instrum.* **2021**, *92*, 63511. [CrossRef]
24. Cao, B.; Pan, Y.; Zhang, W.; Ma, Z.; Sun, L.; Wang, Z. Three-dimensional reconstruction of the excitation temperature of copper atoms in vacuum arcs. In Proceedings of the 2022 6th International Conference on Electric Power Equipment—Switching Technology (ICEPE-ST), Seoul, Republic of Korea, 15–18 March 2022; pp. 45–49, ISBN 2643-9816.
25. Li, Y.; Wang, G.; Liu, J.; Wang, Z.; Wang, J.; Geng, Y.; Liu, Z. 3-D Reconstruction of Vacuum Arc Motion under Transverse Magnetic Fields. In Proceedings of the 2019 5th International Conference on Electric Power Equipment—Switching Technology (ICEPE-ST), Kitakyushu, Japan, 13–16 October 2019; pp. 148–151, ISBN 2643-9816.
26. Khakpour, A.; Franke, S.; Gortschakow, S.; Methling, R.; Popov, S.; Schneider, A.V.; Uhrlandt, D. Investigation of Anode Plume in Vacuum Arcs Using Different Optical Diagnostic Methods. *IEEE Trans. Plasma Sci.* **2019**, *47*, 3488–3495. [CrossRef]
27. Shang, W.; Dullni, E.; Fink, H.; Kleberg, I.; Schade, E.; Shmelev, D.L. Optical investigations of dynamic vacuum arc mode changes with different axial magnetic field contacts. *IEEE Trans. Plasma Sci.* **2003**, *31*, 923–928. [CrossRef]

28. Yu, L.; Pan, B. Single-Camera Stereo-Digital Image Correlation with a Four-Mirror Adapter: Optimized Design and Validation. *Opt. Lasers Eng.* **2016**, *87*, 120–128. [CrossRef]
29. Genovese, K.; Casaletto, L.; Rayas, J.A.; Flores, V.; Martinez, A. Stereo-Digital Image Correlation (DIC) Measurements with a Single Camera using a Biprism. *Opt. Lasers Eng.* **2013**, *51*, 278–285. [CrossRef]
30. Pachidis, T.P.; Lygouras, J.N. Pseudo-Stereo Vision System: A Detailed Study. *J. Intell. Robot Syst.* **2005**, *42*, 135–167. [CrossRef]
31. Comat. PJP Technology. Available online: https://comat.space/en/p/small-sat-en/en-pjp-technology/ (accessed on 10 November 2022).
32. Jarrige, J.; Packan, D.; Blanchet, A.; Herrero, L. Direct Thrust Measurement of a Vacuum Arc Thruster. In Proceedings of the 36th International Electric Propulsion Conference, Vienna, Austria, 15–20 September 2019.